

A Subtropical Cyclonic Gyre Associated with Interactions of the MJO and the Midlatitude Jet

JOHN MOLINARI AND DAVID VOLLARO

Department of Atmospheric and Environmental Sciences, University at Albany, State University of New York, Albany, New York

(Manuscript received 28 February 2011, in final form 18 July 2011)

ABSTRACT

This paper describes a large cyclonic gyre that lasted several days in the northwest Pacific during July 1988. Cyclonic winds at 850 hPa extended beyond the 2000-km radius with a radius of maximum winds of 700–800 km. The gyre exhibited clear skies within and north of its center. Active convection extended 4000 km in longitude to its south.

The Madden–Julian oscillation (MJO) was in its active phase in the Indian Ocean prior to gyre formation. Consistent with earlier studies, diabatic heating in the MJO was associated with an anomalous upper-tropospheric westerly jet over the northeast Asian coast and a jet exit region over the northwest Pacific. Repeated equatorward wave-breaking events developed downwind of the jet exit region. One such event left behind a region of lower-tropospheric cyclonic vorticity and convection in the subtropics that played a key role in the gyre formation. A second wave-breaking event produced strong subsidence north of the mature gyre that contributed to its convective asymmetry.

Gyres from 1985 and 1989 were compared to the 1988 case. All three gyres developed during an active MJO in the Indian Ocean. Each gyre displayed the same strong convective asymmetry. Each developed in July or August during the climatological peak in breaking Rossby waves in the northwest Pacific. Finally, all of the gyres developed during La Niña at nearly the same location. This location and the convective structure of the gyres closely matched composite La Niña anomalies during boreal summer.

1. Introduction

Large low pressure areas that span a significant fraction of the subtropical northwest Pacific are not uncommon in boreal summer. These disturbances are sometimes labeled monsoon depressions (Harr et al. 1996) or monsoon gyres (Lander 1994). Each type of disturbance often has a clear center with light winds that can extend to the 100–200-km radius. Lander (1994, 1996) used the term gyre to distinguish these disturbances from other smaller and more symmetric subtropical lows. The gyre exhibits strong convection on its equatorward and eastern sides (Lander 1994; Molinari et al. 2007). Tropical cyclones often form east of the center and are carried cyclonically around the center by the gyre circulation. Lander (1994) argued that monsoon gyres are fairly uncommon, with one occurring in the

western Pacific every two years on average. Monsoon depressions are more frequent, although no formal study of their number has been carried out for the western Pacific.

The mechanisms responsible for the formation of these gyres remain uncertain. A large monsoon gyre in August 1991 was studied by Lander (1994), Holland (1995), and Molinari et al. (2007). Holland (1995) and Molinari et al. (2007) argued that an equatorward-moving midlatitude trough played a role in the gyre formation by producing a region of persistent diabatic heating near 15°N. The gyre formed to the west of this heating, similar to the idealized solutions of Gill (1980).

Midlatitude disturbances reaching the subtropics are themselves often influenced by the behavior of the Madden–Julian oscillation (MJO) to the west. Matthews and Kiladis (1999) described changes in the structure and evolution of midlatitude jets during an active MJO in boreal winter. These changes resulted in equatorward wave breaking downstream [also labeled anticyclonic wave breaking or “LC1”; Thorncroft et al. (1993)]. The breaking wave produced additional subtropical

Corresponding author address: John Molinari, Department of Atmospheric and Environmental Sciences, ES-225, University at Albany, State University of New York, 1400 Washington Ave., Albany, NY 12222.
E-mail: molinari@atmos.albany.edu

precipitation (Funatsu and Waugh 2008) and equatorial Rossby wave generation. Moore et al. (2010) examined the mean westerly jet at 250 hPa as a function of the MJO state in boreal winter. A mean jet exit region exists in winter near 35°N, 140°W, and equatorward wave breaking maximizes east of the jet exit in the east Pacific. Moore et al. (2010) showed that the jet shifted to the west, along with the wave-breaking region, when the MJO was active over the Indian Ocean. Because the eastern Pacific in boreal winter contains a westerly duct that extends to the equator (Webster and Holton 1982), the breaking Rossby wave trains in that region cross into the Southern Hemisphere (Matthews and Kiladis 1999).

These midlatitude–tropical interactions differ in boreal summer, when the westerly duct rarely exists. Nevertheless, Tam and Li (2006) found evidence for equatorward wave breaking near the date line in boreal summer that played a role in the initiation of lower-tropospheric disturbances. Recently Ding et al. (2011) calculated climatological correlations between boreal summer mean heating over India and 200-hPa mean heights. They found that when a positive seasonal rainfall anomaly occurs over India, a jet is likely to develop over the far northeastern part of Asia, producing an anomalous jet exit region in the northwest Pacific. Postel and Hitchman (1999) found that the annual peak in equatorward wave breaking in the west and central Pacific occurs downwind of this jet during July–September. The papers above suggest that the relationship between the MJO, the midlatitude jet, and downstream wave breaking in boreal summer has some similarities to the more frequently studied events in boreal winter.

The current paper will describe the origin and structure of a cyclonic gyre in the subtropics during July 1988. This gyre was large, long-lasting, and produced intense precipitation over a wide region between 10° and 20°N. Its formation appeared to be tied to the upstream MJO, the midlatitude jet, and multiple wave-breaking events over the northwest Pacific. The scientific questions of interest will be described in section 3.

2. Data sources and calculation methods

Operational gridded analyses from the European Centre for Medium-Range Weather Forecasts (ECMWF) were used to obtain the wind, height, and vorticity fields. Because ocean surface flux calculations were not available from the operational analyses in 1988, those fluxes were taken from the 40-yr ECMWF Re-Analysis (ERA-40) on the same grid resolution. Sea surface temperatures were obtained from the National Oceanic and Atmospheric Administration (NOAA) optimum interpolation analysis (<http://www.esrl.noaa.gov/psd/>). Long-term mean

and anomaly fields at 200 hPa were obtained from the National Centers for Environmental Prediction–National Center for Atmospheric Research (NCEP–NCAR) reanalysis (<http://www.esrl.noaa.gov/psd/data/composites/day/>). Convective activity was evaluated using infrared brightness temperature data from the Cloud Archive User Service (CLAUS), available on a 0.5° latitude–longitude grid 8 times daily.

Similar to McTaggart-Cowan et al. (2008), the dynamical forcing of vertical motion will be defined using \mathbf{Q} -vector divergence (Hoskins et al. 1978). The formulation uses the quasigeostrophic formulation for \mathbf{Q} vectors, but with the geostrophic wind replaced by nondivergent wind (Davies-Jones 1991; see applications by Kiladis et al. 2006; McTaggart-Cowan et al. 2008; Galarneau et al. 2010). This formulation extends the applicability of the results to the subtropics. The \mathbf{Q} vector is given by

$$\mathbf{Q} = (Q_1, Q_2) = -\frac{R}{p} \left(\frac{\partial \mathbf{v}_\psi}{\partial x} \cdot \nabla T, -\frac{\partial \mathbf{v}_\psi}{\partial y} \cdot \nabla T \right), \quad (1)$$

where \mathbf{v}_ψ is the nondivergent wind vector and other variables have their usual meaning. The approach in this paper differs subtly from McTaggart-Cowan et al. (2008) because stability is not incorporated into the definition of \mathbf{Q} , but the results are qualitatively nearly identical. Neglecting the small term involving β (e.g., Holton 2004, chapter 6), the ω equation is given by

$$L(\omega) = -2\mathbf{V} \cdot \mathbf{Q}. \quad (2)$$

Because the operator L contains second derivatives of ω , the left-hand side is proportional to $-\omega$ if fields are sinusoidal (e.g., Holton 2004). As a result, \mathbf{Q} -vector convergence and divergence are associated with upward ($\omega < 0$) and downward motion, respectively. All the results in this paper will show \mathbf{Q} -vector divergence averaged from 400 to 200 hPa.

\mathbf{Q} -vector divergence can be noisy as a result of its proportionality to the second derivative terms noted above. A synoptic-scale forcing for upward and downward motion was desired. As a result, a Gaussian smoother with a 1600-km e -folding distance was applied at each point to the temperature and nondivergent wind components before calculating \mathbf{Q} . The forcing for ascent and descent will be shown to align well with observed cloudy and clear areas, respectively, suggesting that the smoothing is giving physically meaningful results.

3. An acceleration of the zonal wind

Figure 1 shows Hovmöller diagrams of the unfiltered 850-hPa zonal wind and infrared brightness temperature

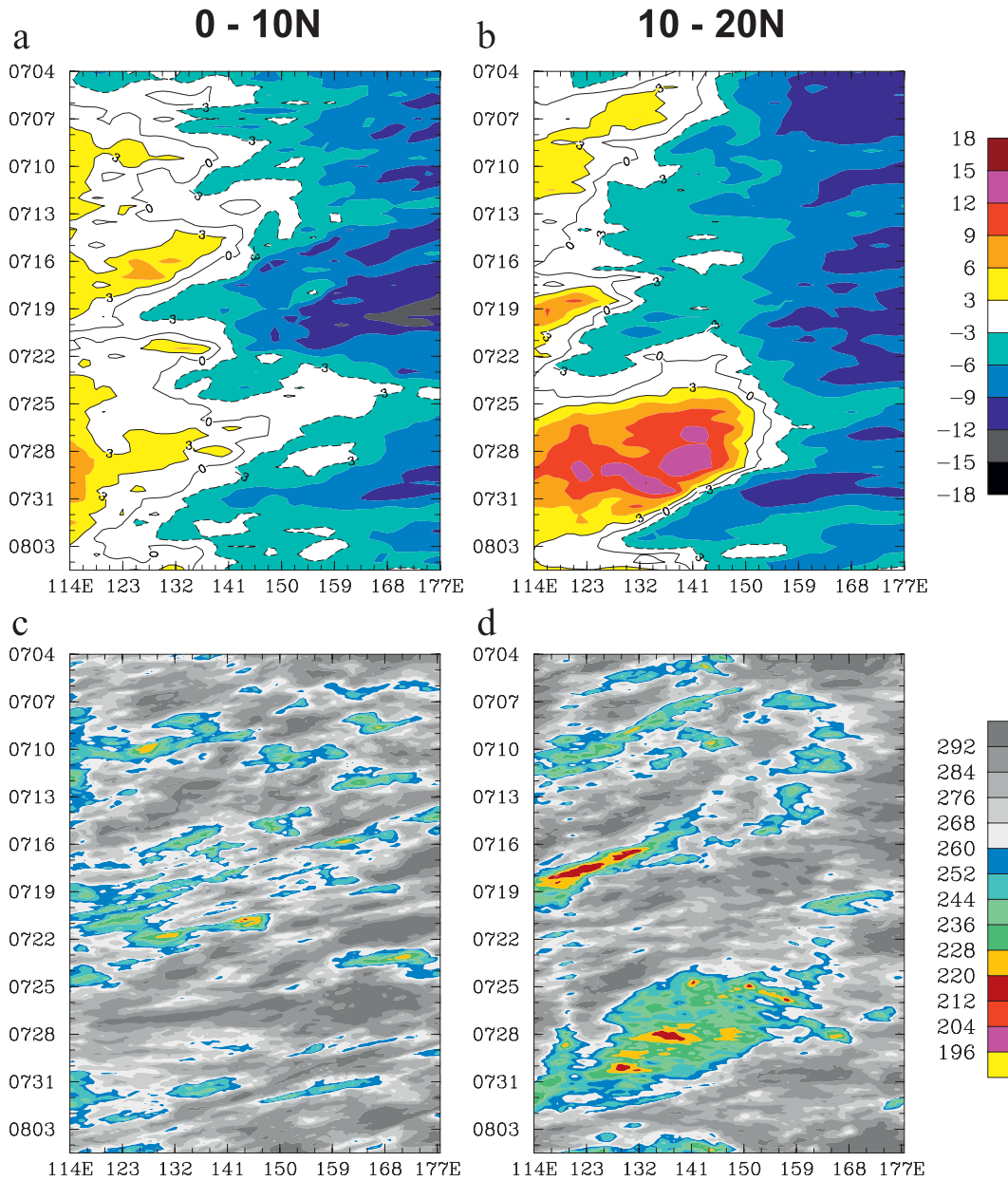


FIG. 1. Longitude–time (Hovmöller) diagram of (top) unfiltered 850-hPa zonal wind (m s^{-1}) and (bottom) infrared brightness temperature (K). (left) Averages from 0° to 10°N and (right) averages from 10° to 20°N. (top) Cool colors are easterlies and warm colors are westerlies. Shading begins at $\pm 3 \text{ m s}^{-1}$ in increments of 3 m s^{-1} .

T_b , each averaged over two latitude bands. The zonal wind over 0°–10°N (Fig. 1a) shows easterly trades from about 140°E to the date line, and weak westerlies west of 140°E. Clear evidence of westward-propagating disturbances was present throughout the period. Their period of roughly 12 days is suggestive of equatorial Rossby waves.

The zonal wind averaged between 10° and 20°N (Fig. 1b) differed considerably. In particular, westerly winds rapidly intensified west of 150°E on 25 July and remained

strong until the end of the month. Mean westerlies over the 10°–20°N latitude belt reached almost 15 m s^{-1} , far stronger than for 0°–10°N.

Figures 1c,d show the T_b Hovmöller diagrams. Consistent with the zonal wind field, westward-propagating waves with alternating convective and nonconvective periods were present at both latitude bands. It is notable, however, that in neither zonal wind nor T_b is there strong evidence of a well-defined wave propagating from upstream between 10° and 20°N prior to the strong

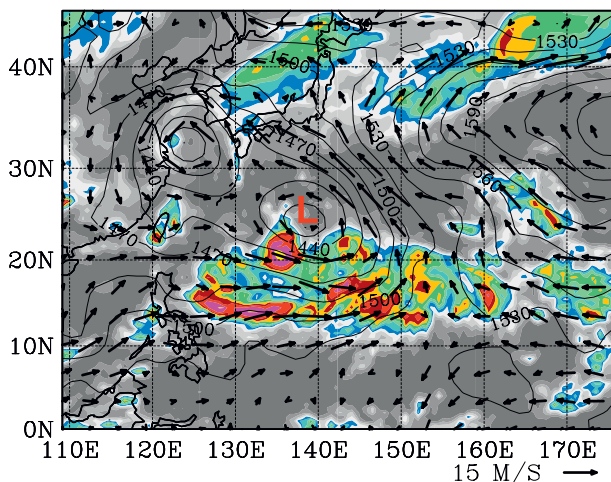


FIG. 2. Infrared brightness temperature (shaded as in Figs. 1c,d) and 850-hPa wind (vectors) and height (contoured in m) for 0000 UTC 27 Jul 1988. The “L” indicates the location of the minimum 850-hPa height at the gyre center.

westerlies. Although the broad mass of cloud moved westward, Fig. 1 suggests that the dramatic feature between 10° and 20°N involved considerably more than the growth of an upstream equatorial Rossby wave.

Figure 2 shows 850-hPa height and wind along with infrared brightness temperature at 0000 UTC 27 July, when the westerlies had reached a maximum near 140°–150°E (Fig. 1b). The strong westerlies were found south of a large cyclonic gyre centered poleward of 20°N. The gyre exhibited strong convection to its south that extended nearly 4000 km in longitude. In contrast, no convection and largely clear skies existed to its north, even near the center. In addition, little or no convection was present in the 0°–10°N latitude band, consistent with Fig. 1c.

Figure 3 shows the radial distribution of azimuthal mean circulation at 850 hPa in the gyre once daily during 27–29 July. Circulation is given by

$$\bar{C} = 2\pi r \bar{v}_\lambda, \quad (3)$$

where v_λ is the tangential velocity and the bar indicates an azimuthal average. Mean circulation was computed by bilinearly interpolating Cartesian winds to a cylindrical grid centered at the surface pressure minimum in the gyre, converting to tangential velocity, and averaging azimuthally at each radius. The circulation field in Hurricane Gloria (1985), which itself was a large tropical cyclone, is shown to indicate the much greater size and stronger circulation of the gyre.

The gyre intensified steadily during the 48-h period while remaining nearly stationary with little change in structure. Circulation increased outward in the gyre,

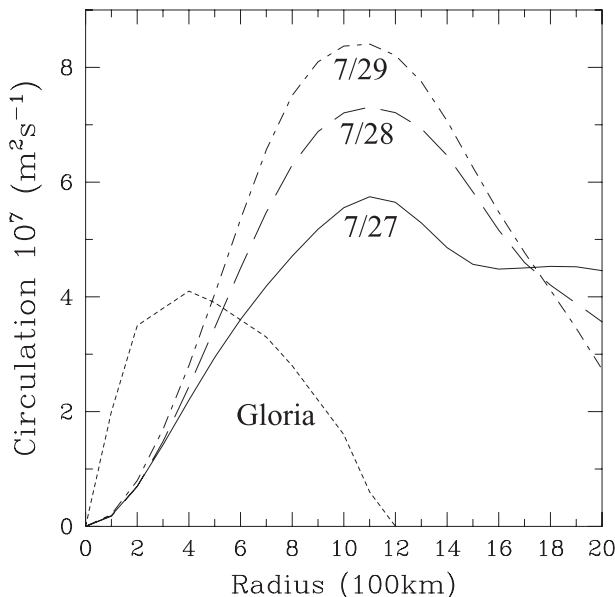


FIG. 3. Azimuthally averaged circulation vs radius at 850 hPa for 0000 UTC 27, 28, and 29 Jul 1988 during the mature stage of the gyre. Circulation in Hurricane Gloria, available only to $r = 1200$ km, is also shown. The Gloria values were determined from tabulated tangential velocity in Mullen et al. (2005, their Fig. 2), which was originally described by Franklin et al. (1993).

which indicates azimuthally averaged cyclonic relative vorticity, from the center to the 1100-km radius. Circulation remained positive, denoting a cyclonic mean tangential wind, beyond the 2000-km radius. The gyre had a radius of maximum winds of 700–800 km throughout the period (not shown), 20 times larger than in Hurricane Gloria. The circulation in Figs. 2–3 was labeled a monsoon depression by the Joint Typhoon Warning Center (JTWC) starting at 0600 UTC 26 July. In this paper it will simply be called a cyclonic gyre following the reasoning of Lander (1994, 1996). The large size of the circulation, with cyclonic winds over a region more than 4000 km in diameter, justifies the use of the “gyre” terminology to distinguish it from an ordinary subtropical low.

Among the questions to be addressed in this paper are the following: (i) how did the gyre form, (ii) why was the gyre so large and so asymmetric, (iii) what were the influences of the upstream MJO and midlatitude jet in its formation and structure, and (iv) what is the possible significance of such gyres in the western Pacific in boreal summer.

4. Subtropical gyre

a. Large-scale background

Figure 4 shows a Hovmöller diagram of 200-hPa meridional wind averaged 30°–40°N over a 2-month period

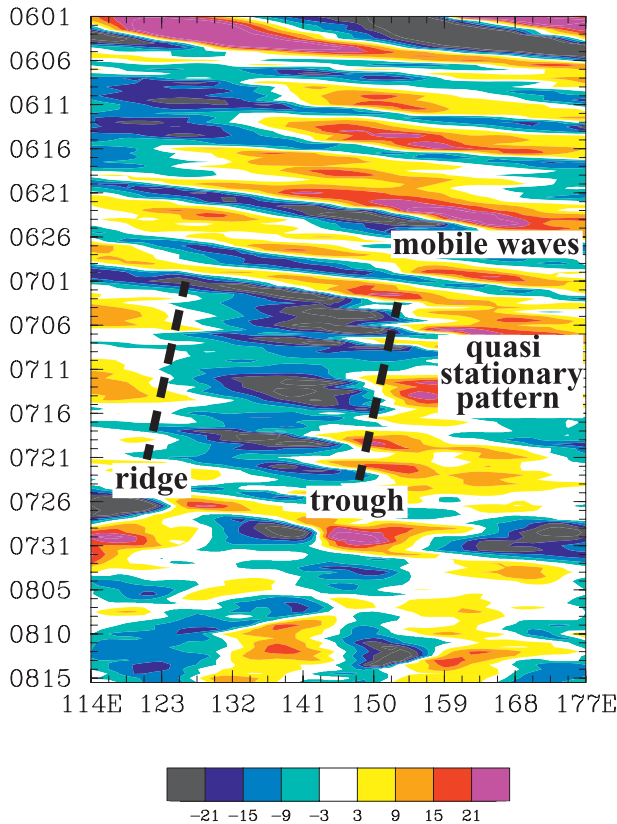


FIG. 4. Hovmöller diagram of 200-hPa meridional wind from early June to mid-August 1988. Values are averaged from 30° to 40°N. Warm colors represent southerlies and cool colors represent northerlies. Shading begins at 3 m s⁻¹ in increments of 6 m s⁻¹.

from early June to mid-August 1988. The month of June was characterized by rapidly eastward-moving, small wavelength midlatitude troughs. In early July, however, a quasi-stationary ridge and trough (with a slow retrogression) became established. It will be shown in later figures that short wavelength disturbances repeatedly turned equatorward out of the 30°–40°N region in the vicinity of the mean trough during July.

Figure 5 shows the mean height and wind at 200 hPa during two consecutive 25-day periods. The first, during 6–30 June (Fig. 5a), represents the time when troughs and ridges propagated eastward. It shows a continuous westerly jet from 35° to 40°N with no jet exit region over the western and central Pacific. The second period, during 1–25 July (Fig. 5b), corresponds to the time when the stationary trough (Fig. 4) was present near 150°E. This period ended just prior to formation of the gyre on 26–27 July. A maximum in the westerly jet developed over Asia about 600 km north of its position in June. The Asian anticyclone also shifted farther north. A jet exit region was present near 145°E upstream of the trough axis. Consistent with Moore et al. (2010), equatorward wave

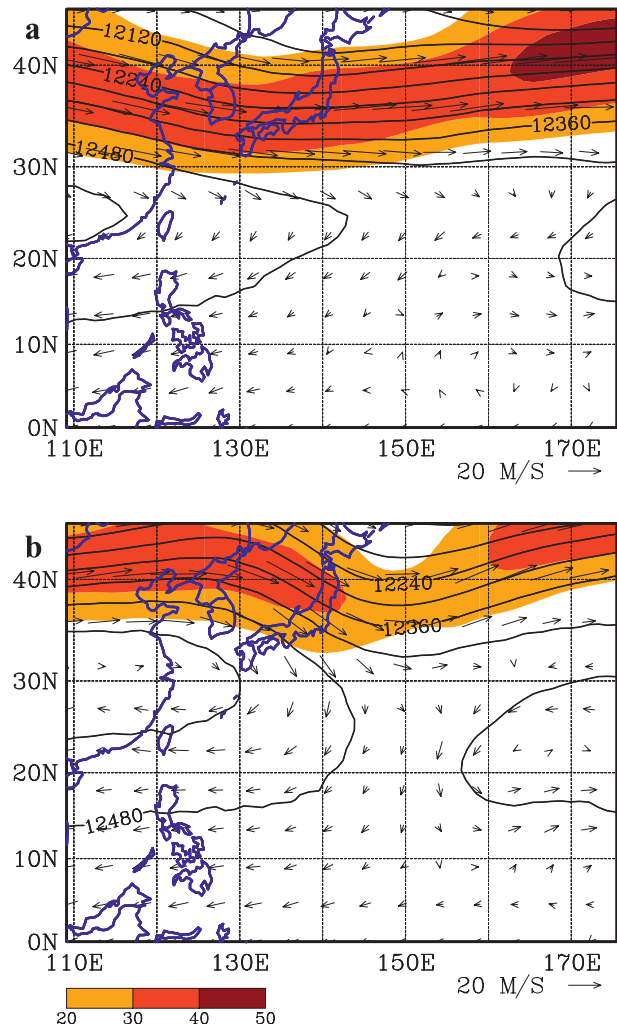


FIG. 5. Mean wind (vectors), wind speed (shading), and height (contours, in m) at the 200-hPa level, averaged from (a) 6–30 Jun and (b) 1–25 Jul 1988. Wind speed shading begins at 20 m s⁻¹ in increments of 10 m s⁻¹.

breaking developed east of the jet exit region, as will be shown later.

A broad trough was also present along 20°N west of the date line during July. This mean trough comprised westward-moving upper-tropospheric lows that usually weakened or stopped moving westward before they reached 150°E. The midtropospheric relative humidity in this region (not shown) remained below 40%, suggesting that the lows did not excite deep cumulus convection and thus did not have substantial dynamical impact on the layers beneath them.

The differences in mean fields over consecutive 25-day periods (Fig. 5) suggest the possible involvement of the MJO. Figure 6 shows a Hovmöller diagram of OLR averaged 7.5°–17.5°N from early June to mid-August 1988. The OLR field is unfiltered except for removal of

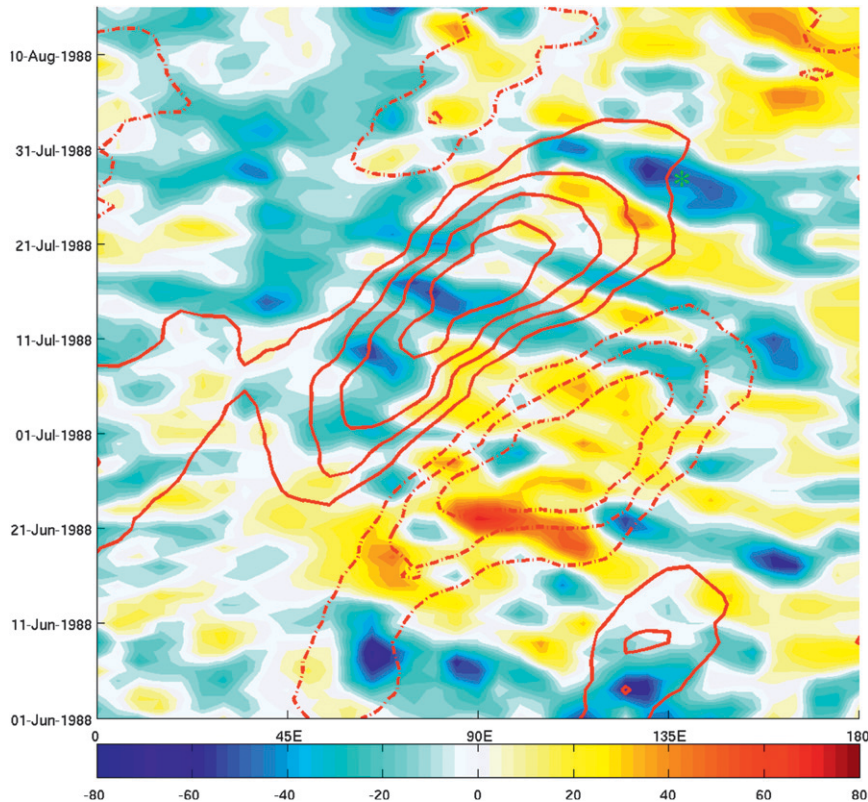


FIG. 6. Longitude–time diagram of OLR (shaded; cool colors represent active convection) and MJO-filtered OLR (red contours; solid represent active MJO, dashed inactive) averaged from 7.5° to 17.5°N . OLR is unfiltered except for removal of the seasonal cycle. This figure follows the procedures of Roundy and Schreck (2009). Roundy’s Web site (see footnote in text) shows the same field throughout 1988 for several additional latitude ranges. The asterisk represents the position of the gyre at 0000 UTC 27 Jul 1988. On this Hovmöller diagram only, time increases upward.

the seasonal cycle. Cool colors represent high clouds and precipitation. Also shown in Fig. 6 are contours of MJO-filtered OLR. This diagram is generated from the time-extended EOF analysis of Roundy and Schreck (2009). The related website (<http://www.atmos.albany.edu/facstaff/roundy/waves/hovs/>) shows images covering the entire globe during 1988 for various latitude ranges. The MJO also shows clearly at 0° – 7.5°N and 2.5° – 12.5°N in those images. It should be noted that time increases upward in Fig. 6, but increases downward in other Hovmöller diagrams in this paper.

The MJO remained inactive in the Indian Ocean during most of June, followed by an active MJO in July. The leading edge of the active MJO reached 135°E before its convective signal decayed. The asterisk in Fig. 6 shows the gyre location at 0000 UTC 27 July, the time of Fig. 2. The gyre formed east of the leading edge of the active MJO.

Figure 5b suggests the presence of significant anomalies in the July mean flow during the active period of the

MJO to the west. Figure 7 shows anomalies from long-term (1968–96) 1–25 July mean 200-hPa winds and height. These anomalies are shown over a larger region than Fig. 5 in order to compare with previous work. The height field shows three anomalous anticyclones between 30° and 40°N , at about 70°E , 120°E , and the date line, with weaker cyclonic anomalies between them. It is far from obvious that this anomaly pattern can be attributed to heating in the MJO over India. However, Ding et al. (2011) showed that during summers with positive rainfall anomalies over India, anomalous anticyclones appeared at virtually the same locations (see their Fig. 9a) as the MJO time-scale anomalies in Fig. 7. They argued for a complex teleconnection process involving synoptic-scale wave propagation and unstable disturbance growth. The similarity of the anomalies in Fig. 7 to those of Ding et al. (2011) suggests that the same process is acting on the MJO scale.

The anomalous anticyclone over northeast Asia and the anomalous cyclone to its east produce an acceleration

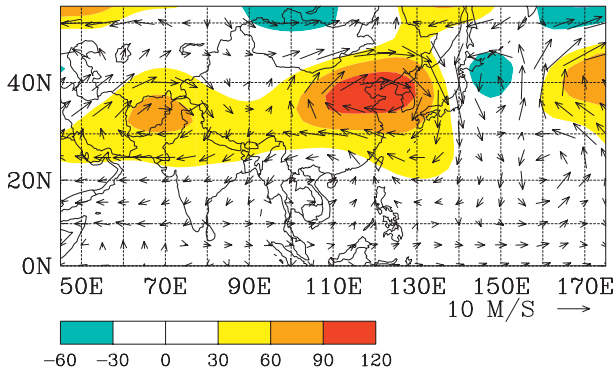


FIG. 7. Anomalies from the long-term mean at 200 hPa averaged during 1–25 Jul 1988 for the horizontal wind (vectors) and height (shaded beginning at ± 30 m in increments of 30 m).

and deceleration, respectively, of the mean westerly jet (cf. anomalous winds in Fig. 7 and mean winds in Fig. 5b). As a result, the development of the jet exit region over the western Pacific in July was directly associated with the anomalies in Fig. 7. Figures 5–7, combined with the strikingly similar anomalies shown by Ding et al. (2011), suggest that the jet exit region over the northwest Pacific, present in July but not in June (Fig. 5), can be attributed to the presence of heating over the Indian region. This result parallels the findings of Moore et al. (2010) for boreal winter.

Figure 8, taken from the paper by Takaya and Nakamura (2001, their Fig. 1), gives some consequences of the presence of the jet exit region in the July mean flow. This work is based on an integration of a barotropic model on a sphere by Enomoto and Matsuda (1999). These authors inserted a Rossby wave source in a mean flow and simulated the evolution of the resulting wave train. The mean flow they used (Fig. 8a) had many similarities to the July mean flow shown in Fig. 5b: the upstream jet maximum slightly exceeded 30 m s^{-1} at a similar latitude; the jet weakened downstream, creating an exit region; an anticyclone was present south of the jet that was associated with easterlies from 20°N to the equator; and a gap in the anticyclone existed at the longitude of the jet exit. The Enomoto and Matsuda (1999) mean flow differed in that westerlies existed all the way to the equator in the jet exit region, creating a westerly duct. In addition, the width of the gap in the jet is larger in their simulation than in Fig. 5b.

The resulting perturbation streamfunction after two weeks of integration is shown in Fig. 8b. Equatorward wave breaking developed at the longitude of the jet exit region, producing a sequence of highs and lows that became oriented southwest–northeast all the way into the Southern Hemisphere. These results are fully consistent with the Moore et al. (2010) finding of maximum

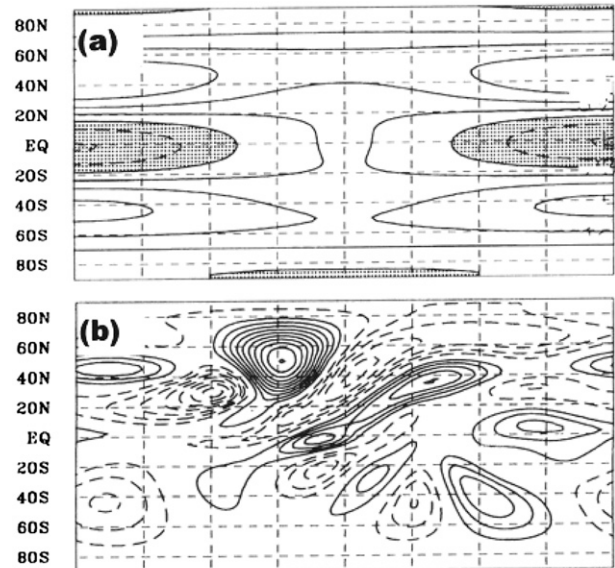


FIG. 8. Idealized simulation of Rossby wave propagation in the presence of a jet exit region, from Takaya and Nakamura (2001, their Fig. 1). (a) Fixed zonal wind during the integration in 10 m s^{-1} increments. Negative values are shaded. (b) Resulting perturbation streamfunction after 2 weeks of integration.

wave breaking east of the jet exit regions in boreal winter.

In the current study, consistent with Takaya and Nakamura (2001), repeated wave-breaking events occurred east of the jet exit region in Fig. 5b during July 1988. These wave-breaking events were defined using the evolution of upper-tropospheric potential vorticity (Funatsu and Waugh 2008). The breaking waves reached their southernmost latitude on 4, 9, 15, 20, and 27 July between 145° and 150°E . Unlike boreal winter examples, the wave train did not cross the equator, but stopped near 20°N . It is hypothesized that the lack of a westerly duct (Fig. 5b) prevented waves from reaching the equator in this case. The last two of the wave-breaking events, on 20 and 27 July, will be discussed in this paper with regard to their roles in the gyre formation and structure, respectively.

b. Gyre formation

The gyre formation process involves events during 19–26 July. Figure 9 shows a sequence of once-daily weather maps from 0000 UTC 19 July to 0000 UTC 24 July, all prior to formation of the gyre. Shown are upper-tropospheric (350-K isentropic surface) Ertel potential vorticity (PV), 350-K winds, and 850-hPa relative vorticity. On 19 July (Fig. 9a), an equatorward wave-breaking event in the upper troposphere was beginning between 140° and 150°E . The intense upper trough centered at 40°N , 146°E was associated with a strong vorticity maximum at 850 hPa

(labeled “*B*”) to its southeast, as would be expected from baroclinic midlatitude dynamics. An 850-hPa vorticity maximum left from a previous wave-breaking event (labeled “*A*”) was present near 25°N, 150°E.

One day later (Fig. 9b), wave breaking continued. Part of 850-hPa vorticity maximum *B* broke off and moved southeastward to 27°N, 140°E. Meanwhile, *A* remained virtually stationary, and *B* and *A* approached one another. By 21 July (Fig. 9c), *B* and *A* were sufficiently close for a mutual interaction, as *B* moved equatorward and *A* moved poleward. A new vorticity maximum near 36°N, 140°E (“*C*”) was associated with the next upper-tropospheric mobile trough.

On 22 July (Fig. 9d), *B* stalled near where *A* stalled earlier, while *C* moved southeastward along a similar track earlier followed by *B*. By 23 July (Fig. 9e), *C* approached *B*, while a new 850-hPa vorticity maximum (“*D*”) appeared at 34°N, 130°E, associated with another mobile trough at higher latitudes. By 24 July (Fig. 9f), *D* intensified near 30°N, 136°E. Meanwhile, *C* and *B* began to interact and merge.

Figure 9 shows that multiple midlatitude lows moved on remarkably similar tracks, moving eastward and equatorward between 130° and 145°E before stalling near 150°E. Figure 10 shows the reasons for this behavior. It displays the mean flow from 1000 to 400 hPa averaged during 19–25 July. Also shown are the locations of vorticity maxima *B* and *D* from Fig. 9f at 0000 UTC 24 July. The longitude of the 1000–400-hPa mean trough in Fig. 10 matches well that for the quasi-stationary 200-hPa trough near 145°E at this time (Fig. 4). This upper trough helped to induce northwesterly flow through a deep layer from 20°–30°N and from 130°–145°E that steered midlatitude vorticity maxima (shown in Fig. 9) equatorward. The confluent zone near 150°E in Fig. 10 marked the region where westerlies associated with the influence of the upper trough met trade wind easterlies. It marked the longitude at which the southeastward-moving midlatitude lows stopped moving eastward (Fig. 9).

Figure 11 picks up where Fig. 9f left off, on 0000 UTC 24 July. Now only 850-hPa wind and vorticity, and infrared brightness temperature, are shown in order to focus on the formation of the gyre. Relative vorticity exceeding $1 \times 10^{-5} \text{ s}^{-1}$ is cross hatched to allow tracking of the broad vorticity structure that became the gyre. Vorticity maxima *D* and *B* (Fig. 11a) were each associated with an area of convection to their east and south. By 0000 UTC 25 July (Fig. 11b), the area of cyclonic vorticity had expanded as the two maxima approached one another. Although *B* was carried poleward, a region of convection to the southeast had grown in size and intensity. Cyclonic vorticity (labeled “*E*”) developed within this convection. Consistent with Gill

(1980), westerlies intensified west of the area of convection.

On 0000 UTC 26 July (Fig. 11c), there was evidence of mutual cyclonic rotation of *D* and *B*, causing *D* to move equatorward and *B* to continue poleward. Vorticity maximum *E* continued to expand within the convective region, as did westerly winds to the west. By 0000 UTC 27 July (Fig. 11d), the same time as shown in Fig. 2, *D* had continued equatorward. The aggregation of *D* and *E*, combined with the strong westerlies to the south, created the extensive vorticity maximum associated with the gyre. The convective region south of the gyre expanded westward into the region of strong westerlies. The gyre continued to intensify over the following two days (Fig. 3), while remaining virtually stationary. Strong convection remained south of the gyre, and largely clear skies to the north, through 29 July.

The somewhat complex gyre formation process can be summarized as follows. The mean upper-tropospheric trough (Figs. 4 and 5b) and jet exit (Fig. 5b) attributed to MJO convection in the Indian Ocean had two primary impacts. First, they were associated with mean northwesterly flow (Fig. 10) through a deep layer to the west that carried midlatitude lower-tropospheric lows equatorward. Second, the jet exit region supported periodic equatorward wave-breaking events east of the trough. The wave-breaking event on 19–22 July left behind a southwest–northeast-tilted region of 350-K PV, lower-tropospheric confluent flow, and persistent convection near 20°N, 150°E. The large gyre arose as a new 850-hPa midlatitude low moved equatorward and interacted and merged with the region of preexisting cyclonic vorticity from the wave-breaking event. It is notable that, with the exception of vorticity generated within the convection (“*E*” in Fig. 11), all of the disturbances involved in this process originated in the midlatitudes.

c. Gyre structure

Because both the gyre and the midlatitude flow patterns were nearly stationary during 27 July (not shown), the gyre structure will be shown as 24-h averages from 0000 UTC 27 July to 0000 UTC 28 July. Convection associated with the gyre (Fig. 12a) represented the dominant subtropical western Pacific feature. Midlatitude T_b showed alternating cloudy and clear regions starting from the northwest corner of the plot eastward and then equatorward, culminating in the strong clear region north of the cyclonic gyre from 22° to 35°N.

Figure 12b shows \mathbf{Q} -vector divergence (shaded) for the 400–200-hPa layer, and 300-hPa streamfunction, each averaged over the same period as in Fig. 12a. This plot shows clear evidence for equatorward wave breaking with alternating forcing for rising motion (warm colors) and

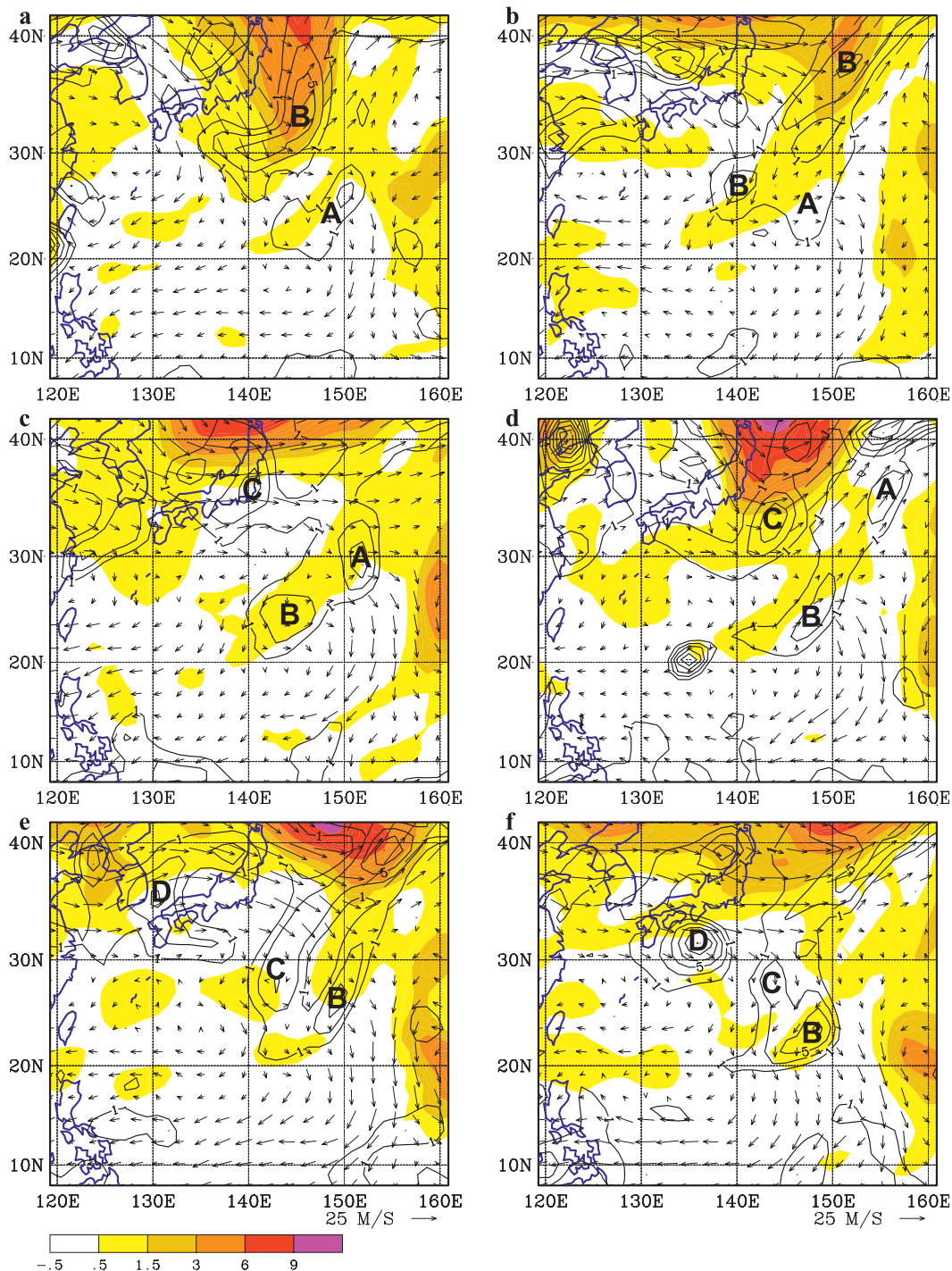


FIG. 9. Potential vorticity on the 350-K isentropic surface (PVU, $1 \text{ PVU} = 10^{-6} \text{ m}^2 \text{ K s}^{-1} \text{ kg}^{-1}$; shaded), 350-K wind (vectors), and 850-hPa vorticity (contours) once daily at 0000 UTC (a) 19 Jul, (b) 20 Jul, (c) 21 Jul, (d) 22 Jul, (e) 23 Jul, and (f) 24 Jul 1988. 850-hPa vorticity is plotted only for values above $1 \times 10^{-5} \text{ s}^{-1}$ in increments of $2 \times 10^{-5} \text{ s}^{-1}$. The uppercase letters follow individual vorticity maxima at 850 hPa.

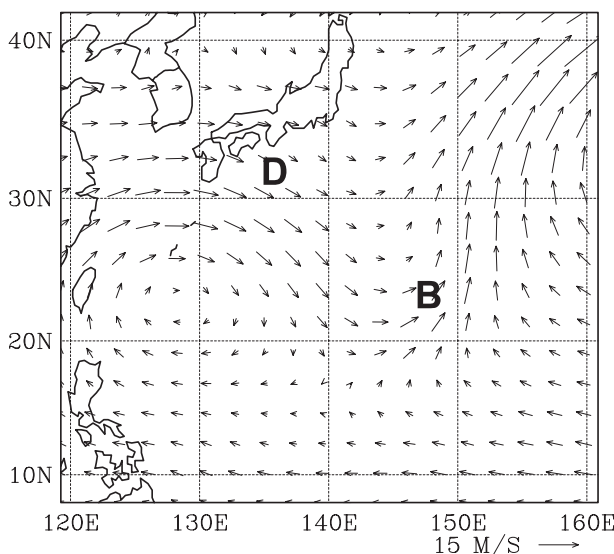


FIG. 10. Mean wind between 1000 and 400 hPa, averaged from 0000 UTC 19 Jul to 0000 UTC 25 Jul 1988, during the time that midlatitude lows moved equatorward and stalled near 150°E. The upper-tropospheric trough line during this period (see Fig. 4) lies along 145°E. The symbols indicate the locations of vorticity maxima D and B at 0000 UTC 24 Jul 1988 (see Fig. 9f).

subsidence (cool colors). These alternating regions extended from the midlatitudes down to a region near 20°N, 150°E that contained persistent upward motion. This wave train became well defined on 26 July and remained until 28 July. It could be tracked back to a region north of 50°N and west of 110°W (not shown).

The wave breaking shown by the \mathbf{Q} -vector forcing in Fig. 12b accounts remarkably well for the clear and cloudy regions in Fig. 12a, in that blue shading for subsidence aligns with clear regions and red shading with cloudy regions. It is notable, however, that the broad region of convection from 10°–20°N to 130°–145°E is not associated with dynamic forcing for upward motion. Figure 13 shows the likely forcing responsible for this latter convective area. It displays sea surface temperature (SST; Fig. 13a) and surface latent and sensible heat flux plotted over the surface wind field (Fig. 13b, averaged over the same times as Fig. 12). The SST distribution (Fig. 13a) was typical for an existing La Niña: it exceeded 29°C west of 160°E and equatorward of 20°N, and decreased slowly to the east and more rapidly to the north. SST exceeded 30°C (dashed contour) in the region where the gyre center developed.

Figure 13b shows that the strong convection south of the gyre center coincided with maxima in surface fluxes, with latent heat flux exceeding 225 W m^{-2} . These maxima resulted from both strong surface winds and high SST values. Surface fluxes were also large northeast of the gyre center (near 25°N, 147°E), but that region remained

clear because it fell within the strong subsidence forced by the breaking waves shown in Fig. 12b.

Figure 14 shows north–south cross sections of zonal wind and Ertel PV through the gyre center (given by the surface pressure minimum), averaged over the same time period as Fig. 12. Cyclonic winds (i.e., easterlies to the north and westerlies to the south) and positive PV extended above the 300-hPa level. Winds and PV varied little in the vertical in that layer. By gradient thermal wind reasoning, this indicates the lack of a radial temperature gradient. As a result, the gyre was not a warm-core disturbance in the lower or midtroposphere. The radius of maximum azimuthally averaged tangential wind (not shown) exceeded 700 km. Zonal winds were stronger in the convective region to the south than in the clear region to the north.

The low tilted southward with height, shown by both the zonal wind and the PV. Mean vertical shear was calculated out to the radius of maximum winds following the method of Corbosiero and Molinari (2002) over the time period represented by Fig. 14. The shear was from the northeast at 5.2 m s^{-1} , consistent with the southward tilt shown in Fig. 14, and with the convective asymmetry shown in Fig. 12a.

d. Impact of the gyre

Figure 15 shows the vertical divergent circulations in the subtropics before and during the gyre lifetime. It displays velocity potential and divergent wind at 150 hPa and mean T_b for two time periods: 1–25 July (Fig. 15a) and 26–29 July (Fig. 15b). During 1–25 July, convection was restricted almost solely to the active MJO in the Indian Ocean, but weak divergent outflow extended over a broad region to the east and west. Figure 15b shows the same fields during the life of the mature cyclonic gyre. The intensity and extent of the divergent outflow were dramatic, even compared to the upstream MJO. Divergent outflow extended to high latitudes in the Northern Hemisphere and across the equator into the Southern Hemisphere. Outflow from the gyre converged at high levels over the Bay of Bengal and appeared to be acting to weaken and/or prevent the propagation of the MJO.

The gyre turned northward as another upper-tropospheric trough approached on 29 August. The JTWC named a tropical cyclone near the center of the gyre at 0000 UTC 29 July. It existed within an elongated 850-hPa vorticity maximum associated with the upper trough. As a result, the disturbance resembled a subtropical cyclone (Davis 2010). This disturbance propagated rapidly toward the high latitudes and was accompanied by considerable amplification of the midlatitude flow downstream. It is beyond the scope of this paper to address the subsequent impacts of the gyre, but evidence

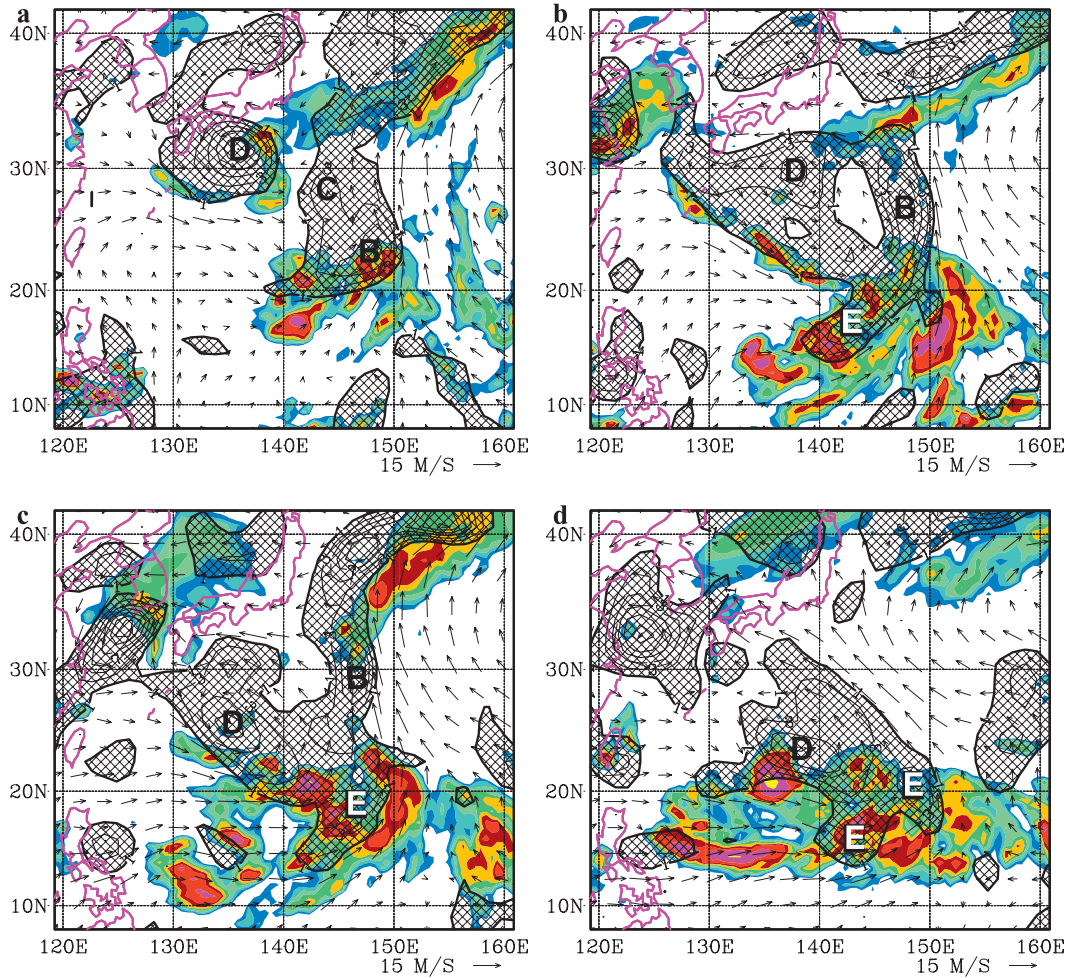


FIG. 11. Wind (vectors) and vorticity (contours) at 850 hPa, and infrared brightness temperature (shaded as in Figs. 1c,d) at 0000 UTC (a) 24 Jul, (b) 25 Jul, (c) 26 Jul, and (d) 27 Jul 1988. The uppercase letters follow individual vorticity maxima at 850 hPa. Vorticity at 850 hPa is plotted only for values above $1 \times 10^{-5} \text{ s}^{-1}$ in increments of $2 \times 10^{-5} \text{ s}^{-1}$. (a) Starts at the same time as in Fig. 9f, and (d) represents the same time as in Fig. 2.

suggests that it had influence well beyond its region of locally enhanced convection.

5. Discussion

a. Gyre formation and structure

The results of this paper suggest that the large, isolated, nearly stationary cyclonic gyre in the western North Pacific in July 1988 had its origin in planetary-scale events. The sequence of events was as follows.

1) Diabatic heating associated with the active MJO over the Indian Ocean helped to create a quasi-stationary upper-tropospheric trough and jet exit region in the northwest Pacific. The mean trough can be seen in Figs. 4 and 5b, and the anomaly fields

in Fig. 7. The jet exit is shown in Fig. 5b and in the anomalies in Fig. 7, and is consistent with the results of Ding et al. (2011).

- 2) The mean trough produced a deep layer of northwesterly flow to its west (Fig. 10) that carried a series of midlatitude lower-tropospheric lows equatorward and eastward (Figs. 9 and 11).
- 3) The jet exit region was associated with repeated equatorward wave-breaking events to its east, consistent with Takaya and Nakamura (2001; see Fig. 8 of this paper), and with Moore et al.'s (2010) study of boreal winter events. One such event from 19–22 July left behind a region of lower-tropospheric confluence near 20°N, 150°E (Fig. 10) where westerlies met trade easterlies. Low pressure areas from the midlatitudes were unable to continue eastward and tended to stall. Persistent convection developed in the confluent zone

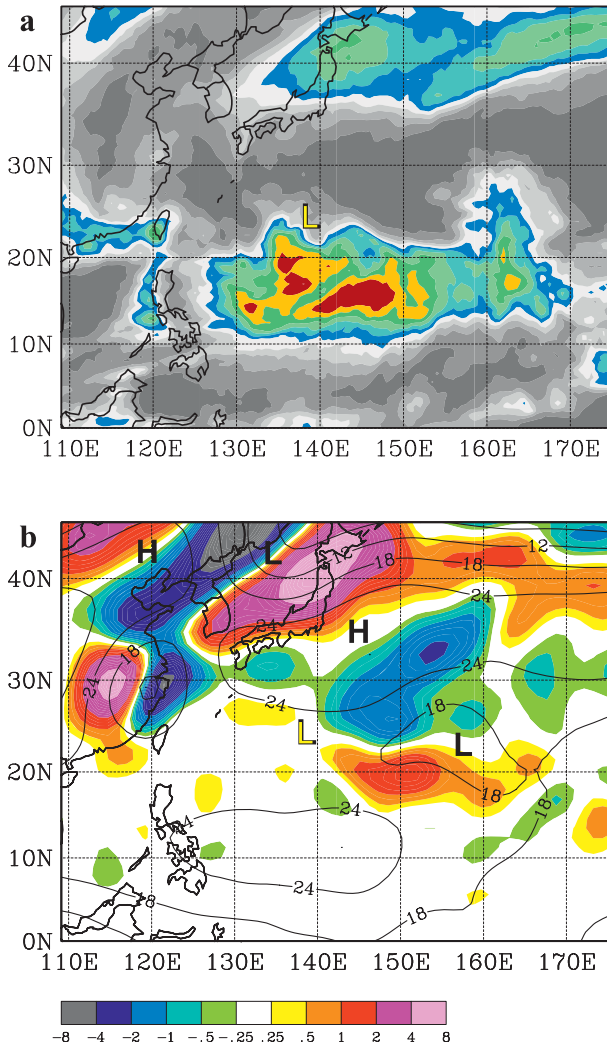


FIG. 12. (a) Mean infrared brightness temperature averaged over 3-hourly periods from 0000 UTC 27 Jul–0000 UTC 28 Jul 1988. Shaded as in Figs. 1c,d. (b) Q -vector divergence for the 400–200-hPa layer (shaded; units of $10^{-18} \text{ m s}^{-1} \text{ kg}^{-1}$) and 300-hPa streamfunction (contours; units $10^6 \text{ m}^2 \text{ s}^{-1}$ with an increment of $6 \times 10^6 \text{ m}^2 \text{ s}^{-1}$), both averaged over the same time period as in (a). Warm colors indicate forcing for rising motion, and cool colors for sinking motion. The yellow “L” indicates the location of minimum central pressure in the gyre during this period.

under a southwest–northeast-oriented strip of 350-K potential vorticity (Figs. 9 and 11).

- 4) The gyre developed as a new midlatitude low at 850 hPa (“D” in Figs. 9–11) moved equatorward and interacted and merged with a growing region of lower-tropospheric vorticity associated with the convection near 20°N, 150°E. The large size of the gyre resulted from the broad region of cyclonic vorticity that evolved from this interaction.
- 5) The persistent convection described above produced an extension of westerly winds to the west, consistent

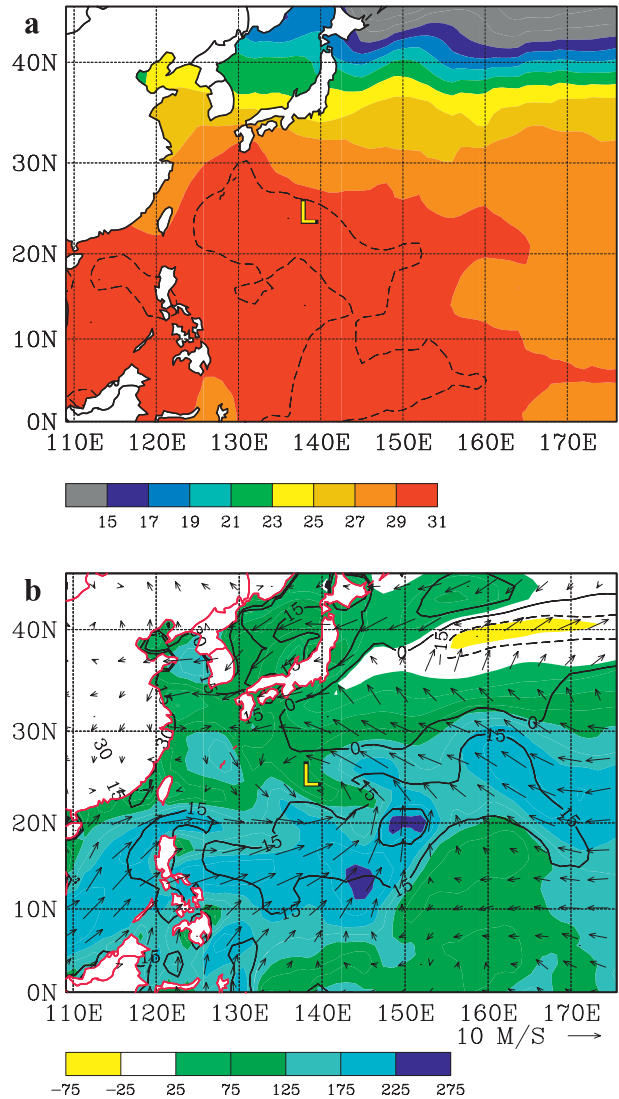


FIG. 13. (a) Mean sea surface temperature over the 7-day period 21–27 Jul 1988, ending just prior to the gyre reaching its mature stage. The dashed contour represents 30°C. (b) Surface latent heat flux (shading), surface sensible heat flux (contours with increment of 15 W m^{-2}), and surface wind (vectors), all averaged over the same period as in Fig. 12. Shading for latent heat flux is in increments of 50 W m^{-2} starting at 25 W m^{-2} . Negative sensible and latent heat fluxes indicate downward flux into the ocean. The yellow “L” indicates the location of minimum central pressure in the gyre during this period.

with the solution of Gill (1980) for steady convection north of the equator. These intensifying westerlies were accompanied by enhanced surface sensible and latent heat fluxes over the warm water (Fig. 13), and a subsequent westward expansion of the deep convection. The result of these events was the large, asymmetric cyclonic gyre shown in Fig. 2.

- 6) A second wave-breaking event on 27–28 July produced strong subsidence north of the mature gyre,

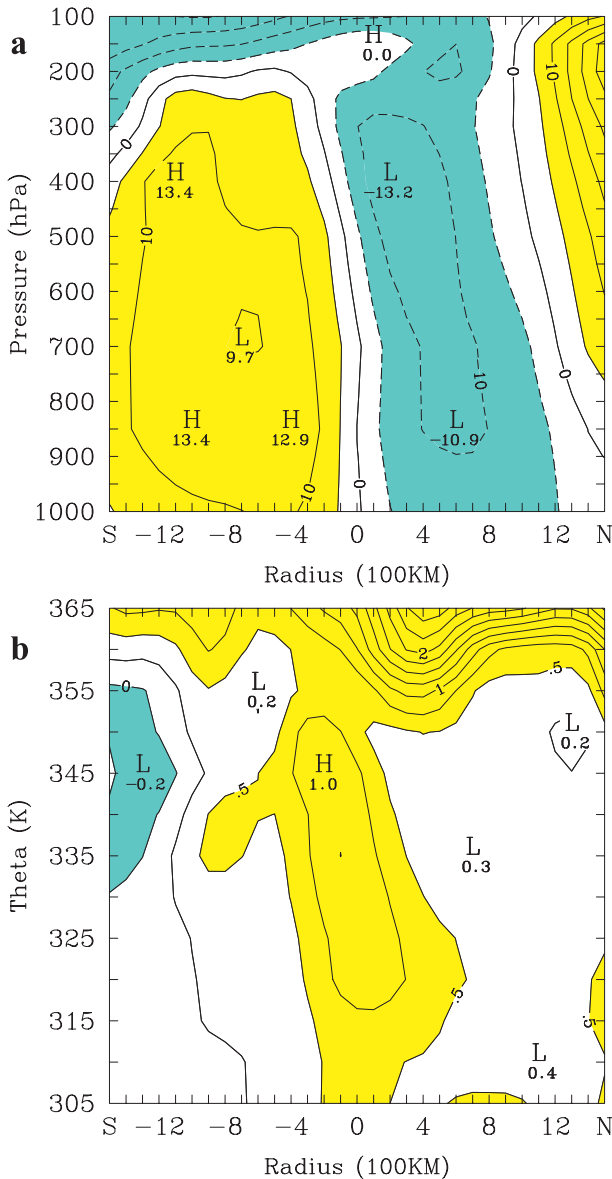


FIG. 14. North-south cross section across the gyre center of (a) zonal wind (m s^{-1}) and (b) Ertel potential vorticity (PVU; $1 \text{ PVU} = 10^{-6} \text{ m}^2 \text{ K s}^{-1} \text{ kg}^{-1}$). In (a), yellow and blue shading represent westerly and easterly winds, respectively, above 5 m s^{-1} . The H indicates a westerly maximum, and the L represents an easterly maximum. In (b), yellow indicates $\text{PV} > 0.5 \text{ PVU}$, and blue $\text{PV} < 0$. Values are averaged from 0000 UTC 27 Jul to 0000 UTC 28 Jul 1988; all are with respect to the gyre center defined by the surface pressure minimum at each time.

accentuating the convective asymmetry that had developed earlier.

The nature of the MJO influence fit the “indirect” forcing described in boreal winter by Matthews and Kiladis (1999) and Moore et al. (2010): the MJO altered the midlatitude flow and allowed equatorward wave breaking

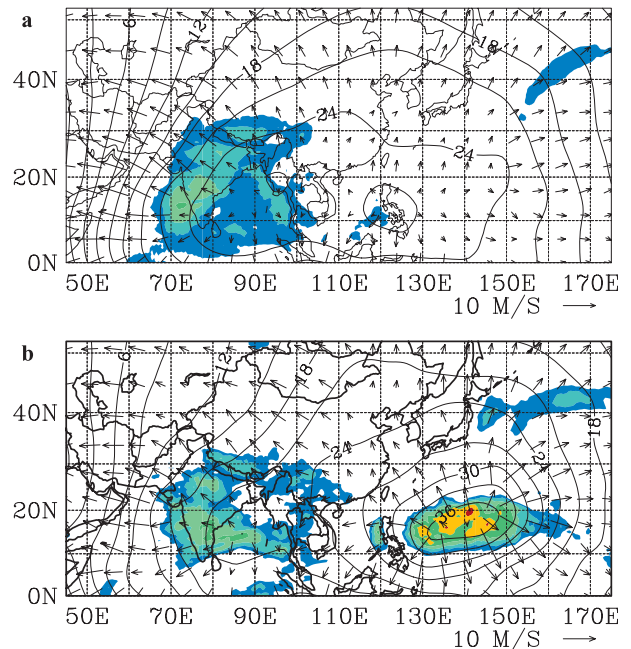


FIG. 15. Velocity potential (contours; increment $3 \times 10^6 \text{ m}^2 \text{ s}^{-1}$) and divergent part of the wind (vectors), both at 150 hPa, and infrared brightness temperature (K; shaded as in Fig. 1), all averaged from (a) 1–25 Jul and (b) 26–29 Jul 1988.

to develop east of the jet exit region as well as the equatorward motion of midlatitude lows west of the mean trough. Much less attention has been paid to midlatitude forcing in boreal summer than in winter. This study, along with those of Postel and Hitchman (1999), Tam and Li (2006), and Ding et al. (2011) suggests that summertime interactions might produce as much response in tropical weather as those in boreal winter.

b. Possible role of equatorial Rossby waves

One unanswered question from this study concerns the role of the westward-propagating waves shown in Fig. 1. These waves did not project well onto equatorial Rossby modes (P. Roundy and C. Schreck 2010, personal communication; see also the plots on Roundy’s Web site noted earlier). Westward-propagating waves from upstream of the gyre did not show in Figs. 1b,d, but did appear to some extent in the OLR in Fig. 6, for which the seasonal cycle had been removed. Such westward-propagating waves would be likely to intensify in the confluent region near 150°E (e.g., Sobel and Bretherton 1999), and it is conceivable that growth of such a wave contributed to development of the gyre. However, Figs. 9 and 11 showed no evidence of vorticity maxima propagating from upstream. In addition, all of the reasoning in this paper showed the dramatic importance of midlatitude forcing in this case. Despite the westward propagation of

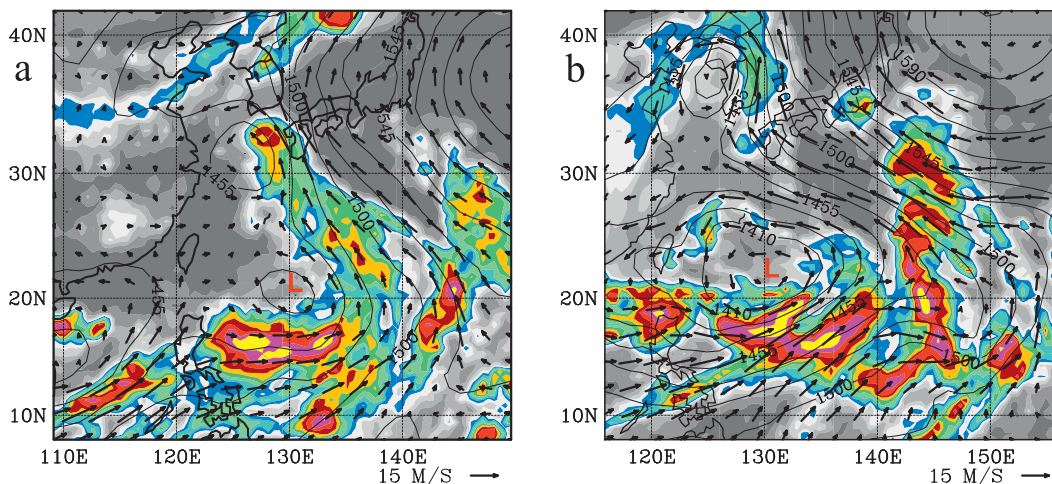


FIG. 16. Two similar gyres to the 1988 example. Plotted as in Fig. 2, but for (a) 0000 UTC 9 Aug 1985 and (b) 0000 UTC 29 Jul 1989.

the cloud mass shown in Fig. 1d, there remains little evidence that equatorial Rossby waves or any other westward-propagating wave from upstream played an important role in the gyre development.

c. Role of cyclonic gyres in the northwest Pacific

An additional question relates to the frequency of large cyclonic gyres. Figure 16 shows two other examples from August 1985 and July 1989. The 1989 gyre was studied by Chen et al. (2004). Each of these gyres was associated with the formation of tropical cyclones. Like the gyre in this study, both gyres in Fig. 16 developed during an active MJO upstream in the Indian Ocean. All three gyres were strongly asymmetric, with relatively little cloudiness within and north of the center, and extensive convection in a region of high winds to its south. All produced extensive precipitation from 10° to 20° N. All were centered within the same 5° latitude by 10° longitude region, and all occurred in July or August. Postel and Hitchman (1999) found that anticyclonic wave breaking of midlatitude Rossby waves peaked in the west Pacific during July–September, suggesting that midlatitude interactions could often play a role in such gyres.

The 1985, 1988, and 1989 gyres occurred during extended periods of negative Niño-3.4 anomalies during La Niña events (<http://www.cpc.ncep.noaa.gov/data/indices/nino34.mth.ascii.txt>). Chen et al. (1998, their Fig. 6b) showed 850-hPa wind and OLR composite anomaly fields in boreal summer during La Niña. A striking cyclonic anomaly was present near 22° N, 137° E, virtually the same location as the three gyres described here. In addition, the OLR field from Chen et al. (1998) showed extensive convection south of the cyclonic anomaly, but not to the north. These examples suggest that large cyclonic

gyres like those described in this paper might be an important component of La Niña in boreal summer. The relationship between these gyres, ENSO, the MJO, and midlatitude flow will be pursued in future work.

Acknowledgments. We are indebted to Dr. Paul Roundy of our department, both for beneficial discussions on the role of the MJO and for creating Fig. 6 of this paper. We also thank Dr. Tom Galarneau of the National Center for Atmospheric Research (NCAR) for help with the software for computing \mathbf{Q} -vector divergence. We appreciate the thoughtful comments from two anonymous reviewers that helped us to clarify the gyre formation process. Gridded analyses from the ECMWF were obtained from NCAR, which is supported by the National Science Foundation (NSF). This work was supported by NSF Grant ATM0839991.

REFERENCES

- Chen, T. C., S. P. Weng, N. Yamazaki, and S. Kiehne, 1998: Interannual variation in the tropical cyclone formation over the western North Pacific. *Mon. Wea. Rev.*, **126**, 1080–1090.
- , S.-Y. Wang, M.-C. Yen, and W. A. Gallus Jr., 2004: Role of the monsoon gyre in the interannual variation of tropical cyclone formation over the western North Pacific. *Wea. Forecasting*, **19**, 776–785.
- Corbosiero, K. L., and J. Molinari, 2002: The effects of vertical wind shear on the distribution of convection in tropical cyclones. *Mon. Wea. Rev.*, **130**, 2110–2123.
- Davies-Jones, R., 1991: The frontogenetical forcing of secondary circulations. Part I: The duality and generalization of the \mathbf{Q} vector. *J. Atmos. Sci.*, **48**, 497–509.
- Davis, C. A., 2010: Simulations of subtropical cyclones in a baroclinic channel model. *J. Atmos. Sci.*, **67**, 2871–2892.
- Ding, Q., B. Wang, J. M. Wallace, and G. Branstator, 2011: Tropical–extratropical teleconnections in boreal summer: Observed interannual variability. *J. Climate*, **24**, 1878–1896.

- Enomoto, T., and Y. Matsuda, 1999: Rossby wavepacket propagation in a zonally-varying basic flow. *Tellus*, **51A**, 588–602.
- Franklin, J. L., S. J. Lord, S. E. Feuer, and F. D. Marks Jr., 1993: The kinematic structure of Hurricane Gloria (1985) determined from nested analyses of dropwindsonde and Doppler radar data. *Mon. Wea. Rev.*, **121**, 2433–2451.
- Funatsu, B. M., and D. W. Waugh, 2008: Connections between potential vorticity intrusions and convection in the eastern tropical Pacific. *J. Atmos. Sci.*, **65**, 987–1002.
- Galarneau, T. J., Jr., L. F. Bosart, and R. S. Schumacher, 2010: Predecessor rain events ahead of tropical cyclones. *Mon. Wea. Rev.*, **138**, 3272–3297.
- Gill, A. E., 1980: Some simple solutions for heat-induced tropical circulation. *Quart. J. Roy. Meteor. Soc.*, **106**, 447–462.
- Harr, P. A., R. L. Elsberry, and J. C. L. Chan, 1996: Transformation of a large monsoon depression to a tropical storm during TCM-93. *Mon. Wea. Rev.*, **124**, 2625–2643.
- Holland, G. J., 1995: Scale interaction in the western Pacific monsoon. *Meteor. Atmos. Phys.*, **56**, 57–79.
- Holton, J. R., 2004: *An Introduction to Dynamic Meteorology*. 4th ed. Elsevier Academic Press, 535 pp.
- Hoskins, B. J., I. Draghici, and H. C. Davies, 1978: A new look at the ω -equation. *Quart. J. Roy. Meteor. Soc.*, **104**, 31–38.
- Kiladis, G. N., C. D. Thorncroft, and N. M. J. Hall, 2006: Three-dimensional structure and dynamics of African easterly waves. Part I: Observations. *J. Atmos. Sci.*, **63**, 2212–2230.
- Lander, M. A., 1994: Description of a monsoon gyre and its effects on the tropical cyclones in the western North Pacific during August 1991. *Wea. Forecasting*, **9**, 640–654.
- , 1996: Specific tropical cyclone track types and unusual tropical cyclone motions associated with a reverse-oriented monsoon trough in the western North Pacific. *Wea. Forecasting*, **11**, 170–186.
- Mallen, K. J., M. T. Montgomery, and B. Wang, 2005: Reexamining the near-core radial structure of the tropical cyclone primary circulation: Implications for vortex resiliency. *J. Atmos. Sci.*, **62**, 408–425.
- Matthews, A. J., and G. N. Kiladis, 1999: The tropical–extratropical interaction between high-frequency transients and the Madden–Julian Oscillation. *Mon. Wea. Rev.*, **127**, 661–677.
- McTaggart-Cowan, R., G. D. Deane, L. F. Bosart, C. A. Davis, and T. J. Galarneau Jr., 2008: Climatology of tropical cyclogenesis in the North Atlantic (1948–2004). *Mon. Wea. Rev.*, **136**, 1284–1304.
- Molinari, J., K. Lombardo, and D. Vollaro, 2007: Tropical cyclogenesis within an equatorial Rossby wave packet. *J. Atmos. Sci.*, **64**, 1301–1317.
- Moore, R. W., O. Martius, and T. Spengler, 2010: The modulation of the subtropical and extratropical atmosphere in the Pacific basin in response to the Madden–Julian oscillation. *Mon. Wea. Rev.*, **138**, 2761–2779.
- Postel, G. A., and M. H. Hitchman, 1999: A climatology of Rossby wave breaking along the subtropical tropopause. *J. Atmos. Sci.*, **56**, 359–373.
- Roundy, P. E., and C. J. Schreck III, 2009: A combined wave-number-frequency and time-extended EOF approach for tracking the progress of modes of large-scale organized tropical convection. *Quart. J. Roy. Meteor. Soc.*, **135**, 161–173.
- Sobel, A. H., and C. S. Bretherton, 1999: Development of synoptic-scale disturbances over the summertime tropical northwest Pacific. *J. Atmos. Sci.*, **56**, 3106–3127.
- Takaya, K., and H. Nakamura, 2001: A formulation of a phase-independent wave-activity flux for stationary and migratory quasigeostrophic eddies on a zonally varying basic flow. *J. Atmos. Sci.*, **58**, 608–627.
- Tam, C.-Y., and T. Li, 2006: The origin and dispersion characteristics of observed tropical summertime synoptic-scale waves over the western Pacific. *Mon. Wea. Rev.*, **134**, 1630–1646.
- Thorncroft, C. D., B. J. Hoskins, and M. E. McIntyre, 1993: Two paradigms of baroclinic-wave life-cycle behavior. *Quart. J. Roy. Meteor. Soc.*, **119**, 17–55.
- Webster, P. J., and J. R. Holton, 1982: Wave propagation through a zonally varying basic flow: The influences of mid-latitude forcing in the equatorial regions. *J. Atmos. Sci.*, **39**, 722–733.